Theor. Comput. Fluid Dyn.
https://doi.org/10.1007/s00162-023-00678-7

ORIGINAL ARTICLE

Alfonso Martínez-Carmena · **Kiran Ramesh**

Inviscid modeling of unsteady morphing airfoils using a discrete-vortex method

Received: 28 February 2023 / Accepted: 26 September 2023
© The Author(s) 2023

Abstract A low-order physics-based model to simulate the unsteady flow response to airfoils undergoing large-amplitude variations of the camber is presented in this paper. Potential-flow theory adapted for unsteady airfoils and numerical methods using discrete-vortex elements are combined to obtain rapid predictions of flow behavior and force evolution. To elude the inherent restriction of thin-airfoil theory to small flow disturbances, a time-varying chord line is proposed in this work over which to satisfy the appropriate boundary condition, enabling large deformations of the camber line to be modeled. Computational fluid dynamics simulations are performed to assess the accuracy of the low-order model for a wide range of dynamic trailing-edge flap deflections. By allowing the chord line to rotate with trailing-edge deflections, aerodynamic loads predictions are greatly enhanced as compared to the classical approach where the chord line is fixed. This is especially evident for large-amplitude deformations.

Keywords Morphing airfoil · Variable camber · Trailing-edge flap · Vortex methods · Thin-airfoil theory · Unsteady aerodynamics · Bio-inspired

1 Introduction

Aerial and aquatic creatures naturally shape their propulsive surfaces, such as wings or tails, to efficiently deal with sudden changes in flow conditions. Drawing inspiration from diverse biological morphing strategies [19], research on bio-inspired locomotion aims to revolutionize the future of micro aerial vehicles (MAVs) and autonomous underwater vehicles (AUVs). Ornithopters, which mimic the morphing and flapping capabilities observed in natural fliers [1,3,10], and fish-like robots that reproduce the undulatory body motion of natural swimmers [41], are expected to enhance the performance envelope of current technologies, improving maneuverability and versatility. However, to explore in depth the flow control capability of morphing techniques over fast-changing flows, in order to beneficially alter the unsteady vorticity field, tools are desired which provide rapid reliable predictions of flow behavior on diverse scenarios. The need of almost real-time estimations of the unsteady flow dynamics renders time-consuming analysis methodologies, like computational fluid dynamics (CFD) simulations or experiments, impractical for this endeavor. A promising alternative is the development of low-order models (LOMs): complex flows are distilled into canonical problems; immersed geometries are simplified; and the use of aerodynamic theories allows the fundamental physics to be captured in a more

Communicated by Vassilis Theofilis.

A. Martínez-Carmena · K. Ramesh (✉)
Aerospace Sciences Division, School of Engineering, University of Glasgow, Glasgow G12 8QQ, Scotland, UK
E-mail: kiran.ramesh@glasgow.ac.uk

A. Martínez-Carmena
E-mail: a.martinez-carmena.1@research.gla.ac.uk

Published online: 07 December 2023

tractable manner [13,31]. Vorticity is often the fluid property chosen to describe the dynamic behavior of unsteady flows, since the flow features of greater interest, like separated shear layers and vortices, can be captured by analyzing the evolution of vorticity fields. Discrete-vortex methods (DVMs) are based on this idea: a continuous distribution of vorticity is discretized into a finite array of computational elements [11]. The Lagrangian nature of these methods allows the flow field to be fully described by tracking the discrete elements according to their local velocities. An extensive review on these numerical methods is given by Spalart [46]. The first studies on vortex methods date back to a century ago, with Rosenhead's investigation on the fundamental problem of free vortex sheets in two dimensions [40]. His ground-breaking research was followed by several attempts to numerically compute the roll-up process of vortex sheets [34,49]. Chorin [7] claimed that discrepancies observed between previous results were due to numerical error and its smoothing effect on the singular character of point vortices. The next fluid problem to be tackled with vortex methods was that of flow separation over bluff bodies and the subsequent vortex shedding process, by initially considering a circular cylinder [43], for which hypotheses are necessary to locate the separation point, and later a squared cylinder [8], whose right angle corners fix the point from which vortex particles enter the flow field. The focus was then moved to flow separation over steady flat plates at high incidence [26,27,44], making use of the Kutta condition to fix the separation point over this geometry. More streamlined geometries were later considered, achieving notable success in the study of cambered airfoils with separation occurring at a given point other than the leading edge [24], which is assumed to be known from experiments. An excellent historical background on the use of vortex methods for the study of two-dimensional vortex sheets is provided by Refs. [9,42], whereas the accuracy and computational efficiency of these methods up to that date is reviewed in Ref. [28]. The use of these vorticity-based methods seemed to wane for some time, but the ever-increasing interest in bio-inspired flight, primarily driven by the advent of micro aerial vehicles, along with the development of computational algorithms for speeding-up simulations [12], have boosted their use in the last decade for rapid estimations of unsteady flows, with some of the earliest models developed in Refs. [2,17,38,52,56]. More recently, discrete-vortex models have been applied to investigate: high-frequency limit-cycle oscillations [39]; energy harvesting efficiency of flapping-foils [23,29]; wing-wake interactions on two-airfoil arrangements [14]; unsteady airfoils encountering external flow disturbances, such as large-amplitude transverse gusts [45], and upstream disturbances generated by a rotating circular cylinder [47]; or the design of airfoil kinematics to modulate vortex shedding characteristics [48]. While research on vortex models for unsteady rigid airfoils is extensive, the effect of chordwise morphing has yet to be addressed with these models. The interest on this practice stems from the extreme degree of deformation observed in the performance of many natural species [4,5,30,35,51,54,55], with the associated benefits for flow control. This has motivated the development of a discrete-vortex model which simulates flow response to foils undergoing large-amplitude camber variations in time. The model sets the groundwork for future investigations on the effect of camber morphing on the unsteady aerodynamics of bio-inspired locomotion from a fundamental viewpoint.

The paper is laid out as follows: The basis of the model is covered in Sect. 2, which includes an extension of thin-airfoil theory for deforming airfoils in Sect. 2.1, aspects of the discrete-vortex scheme in Sect. 2.2, and the derivation of aerodynamic coefficients in Sect. 2.3. Details of the CFD model developed for validation are given in Sect. 3. The performance of the low-order model is tested in Sect. 4, analyzing forces and flow evolution for trailing-edge flap deflections of small amplitude in Sect. 4.1, medium amplitude in Sect. 4.2 and large amplitude in Sect. 4.3. Finally, conclusions are drawn in Sect. 5.

2 Theoretical approach

An existing discrete-vortex model for unsteady rigid wings [37,38] is leveraged and extended in this section to variable-camber wings, giving rise to the so-called morphing discrete-vortex model (MDVM). The underlying mathematics of the theoretical model are described in detail, covering the extension of unsteady thin-airfoil theory (UTAT) to account for temporal camber variations, some aspects of the numerical scheme, and the derivation of the aerodynamic loads.

2.1 Bound vortex sheet

In thin-airfoil theory, an arrangement of elementary solutions is placed over the chord line, whose position and strength are adjusted to satisfy the no-through-flow boundary condition on the aerodynamic surface being

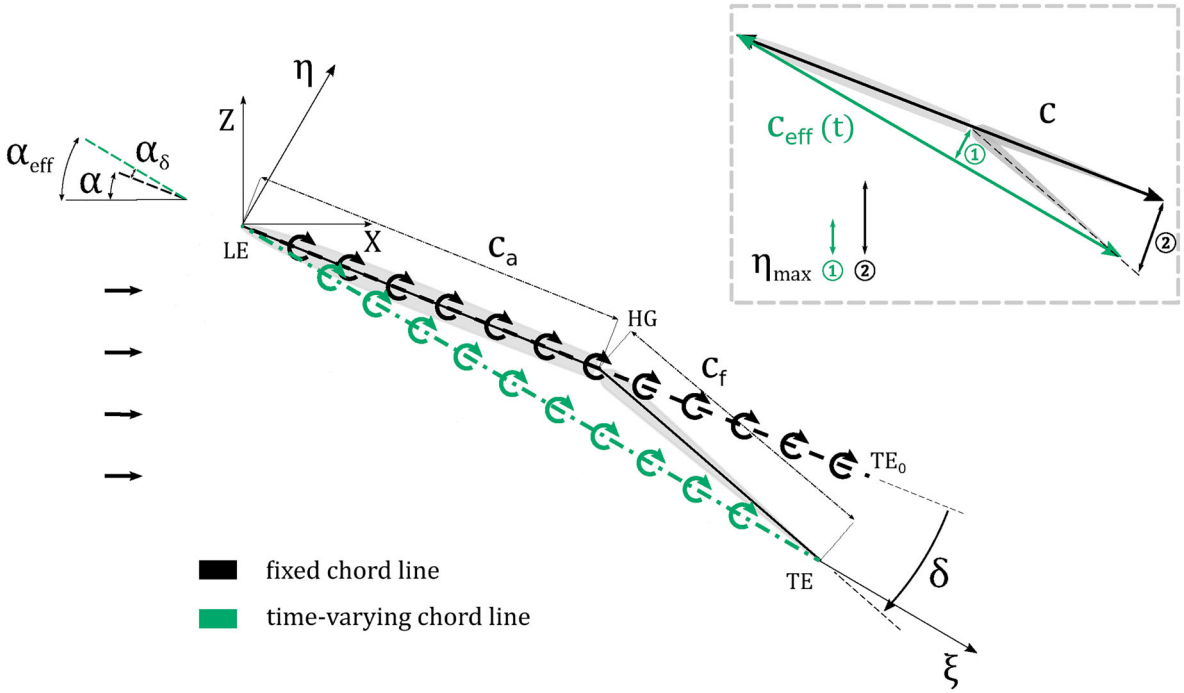

Fig. 1 Schematic of approaches to model a variable-camber airfoil. Round arrows represent distributions of bound vorticity. The inset shows a comparison of the chord line and maximum camber lengths between approaches. Parameters included are defined within the main text

modeled, the camber line in a 2D-problem. Vortex elements are the traditional choice for such basic solutions. The resulting distribution of vorticity represents the vorticity created at the boundary layer and is known as the bound vortex sheet. For a general time-dependent problem, the following trigonometric expansion can be used to approximate the bound vorticity distribution, γ_B:

$$\gamma_B(\theta, t) = 2U_{ref}\left[A_0(t)\frac{1+\cos\theta}{\sin\theta} + \sum_{n=1}^{\infty} A_n(t)\sin(n\theta)\right] \quad , \tag{1}$$

where U_{ref} is a reference velocity; $A_0(t)$,..., $A_n(t)$ are time-dependent Fourier coefficients, expressed as functions of the instantaneous local downwash; t is the time; and θ the variable of transformation used to convert between Cartesian and trigonometric coordinates according to $x = \frac{c}{2}(1-\cos\theta)$, where c is the chord length. At the leading edge $\theta = 0$, and at the trailing edge $\theta = \pi$. The steady Kutta condition (zero vorticity at the trailing edge, $\gamma_B(\pi) = 0$) is implicitly enforced.

2.1.1 Parameters to define morphing

To impose the boundary condition, information is needed on the geometry of the solid surface. In thin-airfoil theory, this shape reduces to the camber line, which for the present work is allowed to vary in time. The most effective way to implement camber morphing in a model is perhaps by acting on the trailing edge, the flapped flat plate being its most basic representation. Here, the camber distribution is given by a piece-wise linear function. Despite its simplicity, this problem establishes the basis for time-varying camber modeling based on potential flow theory and is used throughout the paper.

Following the classical assumption of small disturbances, the boundary condition along the camber line can be transferred to the bound vortex sheet on the chord line to ease the resolution of the problem. This allows the derivation of closed-form expressions for the Fourier coefficients. In a traditional approach, the chord line is the line connecting the airfoil leading and trailing edges at the initial time instant [25], indicated in Fig. 1 with a black dashed line. For the boundary condition to be transferred from the camber line to this chord line, camber must be at every point sufficiently smaller than the chord length. For large deformations, this condition will be violated. This constrains the use of the classical approach to small-amplitude camber variations.

We propose here a time-varying chord line as an alternative approach to overcome said geometric limitation. This effective chord line, c_{eff}, is defined as the line from leading edge to trailing edge at all times, represented in Fig. 1 by a green dash-dotted line. The camber can be expressed in terms of the main element and flap lengths, c_a and c_f, respectively, and the flap deflection angle, δ (positive downward), as:

$$c_{eff}(t) = \sqrt{{c_a}^2 + {c_f}^2 + 2\, c_a\, c_f \cos\delta(t)} \quad . \tag{2}$$

A frame of reference is attached to the camber line, with its origin at the leading edge, one axis running along the effective chord line, and the other perpendicular to it. Points over the camber line are therefore expressed in this frame by their chordwise and normal coordinates, ξ and η, respectively (See Fig. 1).

Owing to the flap deflection, the chord line forms an effective angle of attack, α_{eff}, with the horizontal of an inertial frame, that differs from the pitch angle, α (positive upward), the value of an additional term α_δ. This is, $\alpha_{eff}(t) = \alpha(t) + \alpha_\delta(t)$. For downward flap deflections, the effect of this last contribution is to increase the effective angle of attack, and to reduce it for upward deflections. An expression to define this term is given by:

$$\alpha_\delta(t) = \arcsin\left(\frac{c_f}{c_{eff}(t)}\sin\delta(t)\right) \quad . \tag{3}$$

In the body-fixed frame, the chordwise coordinate is defined in terms of Glauert's transformation variable as:

$$\xi = \frac{c_{eff}}{2}(1 - \cos\theta) \quad . \tag{4}$$

And the camber distribution is expressed by the piece-wise function:

$$\eta(\xi) = \begin{cases} \xi\, \tan\alpha_\delta & \text{for} \quad \xi_{LE} < \xi < \xi_{HG} \quad , \\ (c_{eff} - \xi)\, \tan(\delta - \alpha_\delta) & \text{for} \quad \xi_{HG} < \xi < \xi_{TE} \quad , \end{cases} \tag{5}$$

where $\xi_{LE} = 0$, $\xi_{TE} = c_{eff}$, and $\xi_{HG} = c_a\, cos\alpha_\delta$, are the chordwise coordinates of leading edge, trailing edge and hinge, respectively.

The maximum value of camber in the present model is given for the chordwise coordinate corresponding to the hinge, versus that of the trailing edge in the classical model. If large-amplitude deflections are to be modeled, the camber will be very large at the trailing edge for the fixed chord line approach, and the assumption of small disturbances be violated. By adopting instead the time-varying chord line approach, the maximum camber ratio, $\frac{\eta_{max}}{c}$, is reduced. Thus, the departure from the assumption of small disturbances is diminished and the accuracy on aerodynamic loads prediction is improved. See the inset in Fig. 1 for comparison of the maximum camber value in each model for the same flap deflection amplitude.

2.1.2 Unsteady boundary condition

In unsteady flow problems, time dependency is introduced through the boundary condition. At every point across the fluid–solid interface, zero-normal flow needs to be enforced, $\mathbf{v}\cdot\mathbf{n} = 0$. The velocity of fluid particles is due to body kinematics, surface deformations, external flow perturbations and vortices in the flow field, as detailed in Fig. 2. The sign is the opposite for translation, rotation and deformation terms:

$$\mathbf{v} = -\mathbf{v}_0 - \mathbf{v}_{rot} - \mathbf{v}_{rel} + \mathbf{v}_{ext} + \nabla\boldsymbol{\phi} \quad . \tag{6}$$

Coordinates of each contribution expressed in the body-fixed frame are:

1. Velocity of the origin, due to translation

$$\mathbf{v}_0 = \left(-U\cos\alpha_{eff} - \dot{h}\sin\alpha_{eff}\ ,\ 0\ ,\ -U\sin\alpha_{eff} + \dot{h}\cos\alpha_{eff}\right) \quad . \tag{7}$$

2. Velocity as a rigid body, due to rotation

$$\left.\begin{array}{l} \mathbf{v}_{rot} = \boldsymbol{\Omega}_1 \times \mathbf{r}_1 + \boldsymbol{\Omega}_2 \times \mathbf{r}_2 \\ \boldsymbol{\Omega}_1 = (0\ ,\ \dot{\alpha}\ ,\ 0) \quad , \quad \boldsymbol{\Omega}_2 = (0\ ,\ \dot{\alpha}_\delta\ ,\ 0) \\ \mathbf{r}_1 = \left(\xi - \xi_{pvt}\ ,\ 0\ ,\ \eta - \eta_{pvt}\right) \quad , \quad \mathbf{r}_2 = (\xi\ ,\ 0\ ,\ \eta) \end{array}\right\} \quad . \tag{8}$$

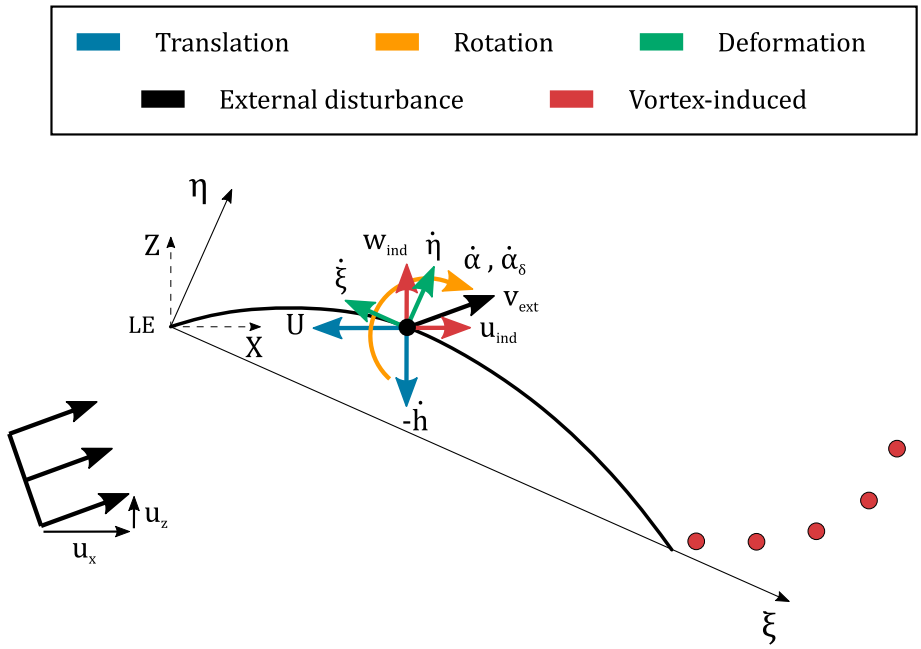

Fig. 2 Decomposition of the velocity at an arbitrary point over the camber line. The orientation of vectors as drawn corresponds to the case described in the main text

3. Relative velocity, due to deformation

$$\mathbf{v}_{rel} = \left(-\dot{\xi}\ ,\ 0\ ,\ \dot{\eta}\right). \tag{9}$$

4. Velocity due to external flow disturbances

$$\mathbf{v}_{ext} = \left(u_x \cos\alpha_{eff} - u_z \sin\alpha_{eff}\ ,\ 0\ ,\ u_x \sin\alpha_{eff} + u_z \cos\alpha_{eff}\right) \quad . \tag{10}$$

5. Velocity induced by vortices

$$\nabla\boldsymbol{\phi} = \left(\frac{\partial\phi_B}{\partial\xi} + \frac{\partial\phi_{TEV}}{\partial\xi} + \frac{\partial\phi_{LEV}}{\partial\xi}\ ,\ 0\ ,\ \frac{\partial\phi_B}{\partial\eta} + \frac{\partial\phi_{TEV}}{\partial\eta} + \frac{\partial\phi_{LEV}}{\partial\eta}\right) \quad . \tag{11}$$

For a generic pitching and plunging case (with no surge motion prescribed), the airfoil translates at a constant velocity along the horizontal axis of an inertial frame, which is taken as the reference velocity, $U_{ref} = U$, plus a plunge velocity in the vertical direction of that same frame, $\dot{h}$. To transform coordinates between body-fixed and inertial frames, the effective angle of attack, α_{eff}, is used. The angular variation terms appearing in the velocity component due to rotation are: the pitch rate about the pivot axis, $\dot{\alpha}$; and the rotation rate of the body-fixed frame about the leading edge owing to trailing-edge flexion, $\dot{\alpha}_\delta$. The coordinates of the pivot axis in the body-fixed frame are $\xi_{pvt} = c_{pvt}\cos\alpha_\delta$ and $\eta_{pvt} = c_{pvt}\sin\alpha_\delta$, with c_{pvt} being the distance between the leading edge and the pivot point. The relative velocity comprises temporal variations of the camber, $\dot{\eta}$, and of the effective chord length, $\dot{\xi}$. To determine the sign of these components note that a positive flap deflection which grows in magnitude increases the camber and reduces the effective chord length. Therefore, for the case of $\delta > 0$ with $\dot{\delta} > 0$ we have $\dot{\eta} > 0$ and $\dot{\xi} < 0$. Without loss of generality, we assume in this work that there are no external flow disturbances, $u_x = u_z = 0$. Finally, it must be stressed that the bound vorticity, the trailing-edge vorticity, and the leading-edge vorticity all contribute a component to the velocity potential, $\phi = \phi_B + \phi_{TEV} + \phi_{LEV}$. Thence, $\frac{\partial\phi}{\partial\xi}$ and $\frac{\partial\phi}{\partial\eta}$ represent velocities induced by each of these vortices tangential and normal to the effective chord line, respectively.

Temporal derivatives in Eqs. (7) to (11) are calculated as:

$$\dot{\alpha}_\delta = \frac{\cos\delta + \frac{c_a}{c_{eff}}\frac{c_f}{c_{eff}}\sin^2\delta}{\frac{c_a}{c_f} + \cos\delta}\dot{\delta} \quad , \tag{12a}$$

$$\dot{\xi} = \xi \frac{\dot{c}_{eff}}{c_{eff}} = -\xi \frac{\eta_{max}}{c_{eff}} \dot{\delta} \quad , \tag{12b}$$

$$\dot{\eta} = \begin{cases} \tan\alpha_\delta \dot{\xi} + \dfrac{\xi}{\cos^2\alpha_\delta}\dot{\alpha}_\delta & \text{for } \xi < \xi_{HG} \ , \\ \left(\dfrac{\xi}{c_{eff}} - 1\right)\eta_{max}\tan(\delta - \alpha_\delta)\dot{\delta} + \dfrac{c_{eff} - \xi}{\cos^2(\delta - \alpha_\delta)}(\dot{\delta} - \dot{\alpha}_\delta) & \text{for } \xi > \xi_{HG} \ , \end{cases} \tag{12c}$$

where $\dot{\delta}$ represents the rate of flap deflection.

Vortex-induced velocities in Eq. (11) are converted from their expression in an inertial frame:

$$\frac{\partial \phi}{\partial \xi} = u_{ind}\cos\alpha_{eff} - w_{ind}\sin\alpha_{eff} \quad , \tag{13a}$$

$$\frac{\partial \phi}{\partial \eta} = u_{ind}\sin\alpha_{eff} + w_{ind}\cos\alpha_{eff} \quad , \tag{13b}$$

with their components in the inertial x and z directions, u_{ind} and w_{ind}, respectively, provided by the Biot–Savart law.

To apply the boundary condition, the normal vector to the surface of interest, here the camber line, is needed. The unit normal vector to this curve (positive outward) can be obtained from its implicit representation as:

$$\mathbf{n} = \frac{1}{\sqrt{1 + \left(\frac{\partial \eta}{\partial \xi}\right)^2}}\left(-\frac{\partial \eta}{\partial \xi}, 0, 1\right) \quad , \tag{14}$$

where $\frac{\partial \eta}{\partial \xi}$ represents the slope of the camber line.

Upon defining the velocity vector of a fluid particle at an arbitrary location over the camber line, by adding all the contributions from Eqs. (7) to (11), and using the normal vector given in Eq. (14) to enforce the boundary condition, the instantaneous local downwash, $\frac{\partial \phi_B}{\partial \eta}$, is yielded. Its general form, for an arbitrary foil flapping and deforming simultaneously in a vortex-dominated scenario, is:

$$\begin{aligned} W(\xi, t) = \frac{\partial \eta}{\partial \xi}\Bigg(&\frac{\partial \phi_{TEV}}{\partial \xi} + \frac{\partial \phi_{LEV}}{\partial \xi} + U\cos\alpha_{eff} + \dot{h}\sin\alpha_{eff} - \dot{\alpha}(\eta - \eta_{pvt}) - \dot{\alpha}_\delta \eta + \dot{\xi}\Bigg) \\ &- \frac{\partial \phi_{TEV}}{\partial \eta} - \frac{\partial \phi_{LEV}}{\partial \eta} - U\sin\alpha_{eff} + \dot{h}\cos\alpha_{eff} - \dot{\alpha}(\xi - \xi_{pvt}) - \dot{\alpha}_\delta \xi + \dot{\eta} \quad . \end{aligned} \tag{15}$$

Note that the term $\frac{\partial \phi_B}{\partial \xi}$ has been neglected in the above expression, since it is an order of magnitude smaller than the rest of terms.

The Fourier coefficients, and by extension the distribution of bound vorticity introduced in Eq. (1), are dependent on the instantaneous shape of the camber line through the downwash expression:

$$A_0(t) = -\frac{1}{\pi}\int_0^\pi \frac{W(\xi, t)}{U_{ref}} d\theta \quad , \tag{16a}$$

$$A_n(t) = \frac{2}{\pi}\int_0^\pi \frac{W(\xi, t)}{U_{ref}}\cos(n\theta) d\theta \quad . \tag{16b}$$

These coefficients are finally used to define the bound circulation. After integrating the bound vorticity distribution over the time-varying chord line:

$$\Gamma_B(t) = \pi c_{eff} U_{ref}\left(A_0(t) + \frac{A_1(t)}{2}\right) \quad . \tag{17}$$

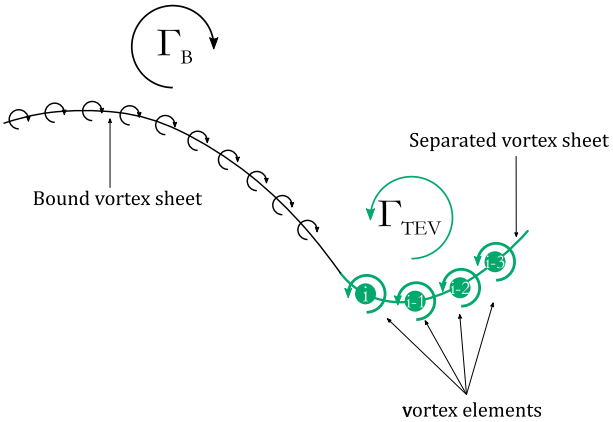

Fig. 3 Discrete representation of a separated vortex sheet at the trailing edge of an unsteady airfoil using vortex elements

2.2 Separated vortex sheets

As the airfoil moves following a prescribed trajectory and the flap is deflected, a free vortex sheet forms at the trailing edge. Vortex methods approximate these sheets by arrays of vorticity-carrying elements, depicted in Fig. 3. In this model, a time-stepping scheme is implemented to determine the amount of elements comprising the vortex sheet, as outlined in Refs. [25,37,38]. A vortex particle is therefore shed from the trailing edge at every time step of the numerical simulation. These computational elements are treated as vortex blobs rather than point vortices [6], by including the core radius of the blob in the calculation of induced velocities to regularize the interactions between all elements. The vortex-core model adopted is that proposed in Ref. [50].

The Biot–Savart law provides the inertial components of the velocity induced by each vortex blob at any point along the camber line:

$$u_{ind} = \frac{\Gamma_k}{2\pi} \frac{z - z_k}{\sqrt{\left((x - x_k)^2 + (z - z_k)^2\right)^2 + v_{core}^4}} \quad , \tag{18a}$$

$$w_{ind} = -\frac{\Gamma_k}{2\pi} \frac{x - x_k}{\sqrt{\left((x - x_k)^2 + (z - z_k)^2\right)^2 + v_{core}^4}} \quad , \tag{18b}$$

where Γ_k is the strength of the vortex blob; v_{core} its core radius; (x_k, z_k) its coordinates; and (x, z) those of the point where velocities are computed.

The strength assigned to vortex elements shed from the trailing edge can be calculated in different ways. An iterative process is often used, so Kelvin's circulation conservation theorem is satisfied. This theorem establishes a relation between vortex sheets:

$$\frac{d\Gamma_B(t)}{dt} + \frac{d\Gamma_{LEV}(t)}{dt} + \frac{d\Gamma_{TEV}(t)}{dt} = 0 \quad . \tag{19}$$

As already mentioned, no leading-edge vorticity shedding is considered in this paper, $\Gamma_{LEV} = 0$. On the other hand, the bound circulation, Γ_B, is given by Eq. (17). It is therefore straightforward to compute the strength of vortex blobs shed from the trailing edge.

In scenarios with continuous shedding of trailing-edge vorticity, the use of vortex blobs to represent the vorticity shed at any time step results in a discontinuity in the vortex sheet across this edge, giving an erroneous solution. An alternative approach that eliminates this error is to represent said vorticity as a continuous distribution derived from the exact Wagner solution. After obtaining the solution at each time step, this vorticity is converted into a vortex blob placed at the centroid of the distribution. More details on the implementation are provided in Ref. [36]. Results from MDVM using both approaches are compared in Sect. 4.1 to illustrate the difference.

To guarantee convergence of the discrete-vortex method, the vortex-core radius needs to be larger than the average spacing between blobs, $d = \Delta t U$, and $v_{core} = 1.3d$ is here taken following guidelines from Ref. [28]. A non-dimensional time step $\Delta t^* = \frac{\Delta t U}{c} = 0.015$ is used for the results shown in Sect. 4, giving a core radius

$\frac{v_{core}}{c} = 0.02$. The last shed vortex blob is placed at one third of the distance from the trailing edge to the previously shed particle [2]. This enables a more accurate depiction of the flow, since the effect of the airfoil's motion and the advection of the previous vortex blob are both being accounted for. The vortex blobs in the flow field are convected with the net velocity induced at their center (summation of mutual interactions and free stream). This enables the wake to roll-up into vortex structures.

2.3 Aerodynamic coefficients

If the velocity field is known, Bernoulli's equation modified for the unsteady regime provides the pressure difference over the airfoil:

$$\Delta p(\xi) = p_l(\xi) - p_u(\xi) = \rho \left[\frac{1}{2}(V_{t_u}^2 - V_{t_l}^2) + \left(\frac{\partial \phi}{\partial t}\right)_u - \left(\frac{\partial \phi}{\partial t}\right)_l \right] \quad . \tag{20}$$

Following a similar reasoning to that in Ref. [38] applied to the present problem, the pressure distribution over the airfoil evaluates to:

$$\begin{aligned} \Delta p(\xi) = \rho \Big[\Big(& \frac{\partial \phi_{TEV}}{\partial \xi} + \frac{\partial \phi_{LEV}}{\partial \xi} + U \cos \alpha_{eff} + \dot{h} \sin \alpha_{eff} \\ & - \dot{\alpha}(\eta - \eta_{pvt}) - \dot{\alpha}_\delta \eta + \dot{\xi} \Big) \gamma(\xi) + \frac{\partial}{\partial t} \int_0^\xi \gamma(\xi) d\xi \Big] \quad . \end{aligned} \tag{21}$$

The normal force on the airfoil is obtained by integrating Eq. (21) over the chord line, and $\frac{1}{2}\rho U_{ref}^2 c$ is used to normalize it. The different contributions to the normal force coefficient are broken down below:

1. Non-circulatory

$$C_{N_{nc}} = \frac{2\pi c_{eff}^2}{Uc} \left(\frac{3}{4}\dot{A}_0(t) + \frac{1}{4}\dot{A}_1(t) + \frac{1}{8}\dot{A}_2(t) \right). \tag{22}$$

2. Circulatory due to translation

$$C_{N_t} = \frac{2\pi c_{eff}}{Uc} \Big(U \cos \alpha_{eff} + \dot{h} \sin \alpha_{eff} \Big) \left(A_0(t) + \frac{1}{2} A_1(t) \right). \tag{23}$$

3. Circulatory due to rotation

$$C_{N_r} = -\frac{2}{U^2 c} \int_0^{c_{eff}} \Big(\dot{\alpha}(\eta(\xi) - \eta_{pvt}) + \dot{\alpha}_\delta \eta(\xi) \Big) \gamma(\xi) d\xi. \tag{24}$$

4. Circulatory due to deformation

$$C_{N_d} = \frac{2}{U^2 c} \int_0^{c_{eff}} \dot{\xi} \gamma(\xi) d\xi. \tag{25}$$

5. Circulatory caused by vortices

$$C_{N_v} = \frac{2}{U^2 c} \int_0^{c_{eff}} \left(\frac{\partial \phi_{TEV}}{\partial \xi} + \frac{\partial \phi_{LEV}}{\partial \xi} \right) \gamma(\xi) d\xi. \tag{26}$$

Note that deflection of the flap has two contributions: varying the effective angle of attack by $\dot{\alpha}_\delta$, and varying the effective chord length by $\dot{\xi}$.

In addition to this pressure force, a suction force acts axial to the airfoil in the upstream direction, which is given by the Blasius formula. The previous factor is used to obtain the suction force coefficient:

$$C_S = 2\pi A_0^2 \quad . \tag{27}$$

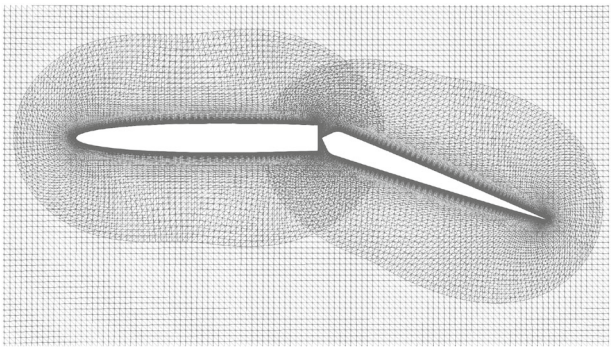

Fig. 4 Detail of the overset-mesh strategy adopted for the airfoil-flap configuration: body-fitted meshes for both elements and background mesh

Combining these two aerodynamic forces, the lift and drag coefficients are expressed in the free stream coordinate system as:

$$C_L = C_N \cos\alpha_{eff} + C_S \sin\alpha_{eff} \quad , \tag{28a}$$

$$C_D = C_N \sin\alpha_{eff} - C_S \cos\alpha_{eff} \quad . \tag{28b}$$

Finally, the pitching moment coefficient (nose-up positive) is obtained by integrating the product of pressure force and position vector (distance from the pivot axis to the point where the force is applied) over the chord line. Using $\frac{1}{2}\rho U_{ref}^2 c^2$ to normalize it:

$$\begin{aligned} C_M = {} & C_N \frac{c_{pvt}}{c}\cos\alpha_\delta - \frac{2\pi c_{eff}^2}{Uc}\left(\frac{7}{16}\dot{A}_0(t) + \frac{11}{64}\dot{A}_1(t) + \frac{1}{16}\dot{A}_2(t) - \frac{1}{64}\dot{A}_3(t)\right) \\ & - \frac{2\pi c_{eff}^2}{Uc^2}\left(U\cos\alpha_{eff} + \dot{h}\sin\alpha_{eff}\right)\left(\frac{1}{4}A_0(t) + \frac{1}{4}A_1(t) - \frac{1}{8}A_2(t)\right) \\ & + \frac{2}{U^2c^2}\left[\int_0^{c_{eff}}\left(\dot{\alpha}(\eta(\xi) - \eta_{pvt}) + \dot{\alpha}_\delta\eta(\xi) - \dot{\xi} - \frac{\partial\phi_{TEV}}{\partial\xi} - \frac{\partial\phi_{LEV}}{\partial\xi}\right)\gamma(\xi)\xi d\xi\right] . \end{aligned} \tag{29}$$

3 Computational approach

The reference data used in this work to validate the low-order model have been obtained from high-fidelity computational fluid dynamic simulations. A CFD model for airfoils equipped with a dynamic trailing-edge flap was designed using an in-house version of OpenFOAM [16,21]. Experimental data available in the literature [33] were used to create the geometry of the airfoil for the mesh, and to validate the performance of the new CFD model. The geometry consists of a NACA 0006 profile with a trailing-edge flap hinged at its mid-chord. The total chord length of this configuration is 20cm.

A structured overset grid was built to enable the kinematics to be prescribed independently for each moving part of this multi-body configuration. The resultant mesh consists of two body-fitted meshes and a background mesh, as illustrated in Fig. 4.

CFD simulations were performed with the following set-up: the finite volume method to solve the time-dependent incompressible Navier-Stokes equations; a second-order backward implicit scheme to discretize the time derivatives; second-order limited Gaussian integration schemes for the gradient, divergence and Laplacian terms; the PISO algorithm to achieve pressure–velocity coupling; and the Spalart–Allmaras turbulence model for turbulence closure.

Kinematics used in experimental work were recreated for validation. The main element was fixed at $\alpha = 0°$, and a smoothed ramp-hold motion was prescribed to the trailing-edge flap (see Ref. [33]) with amplitude $\delta = 20°$ and three reduced rates of flap deflection: $K_\delta = 0.07$ (slow), $K_\delta = 0.27$ (medium) and $K_\delta = 1.09$ (fast).

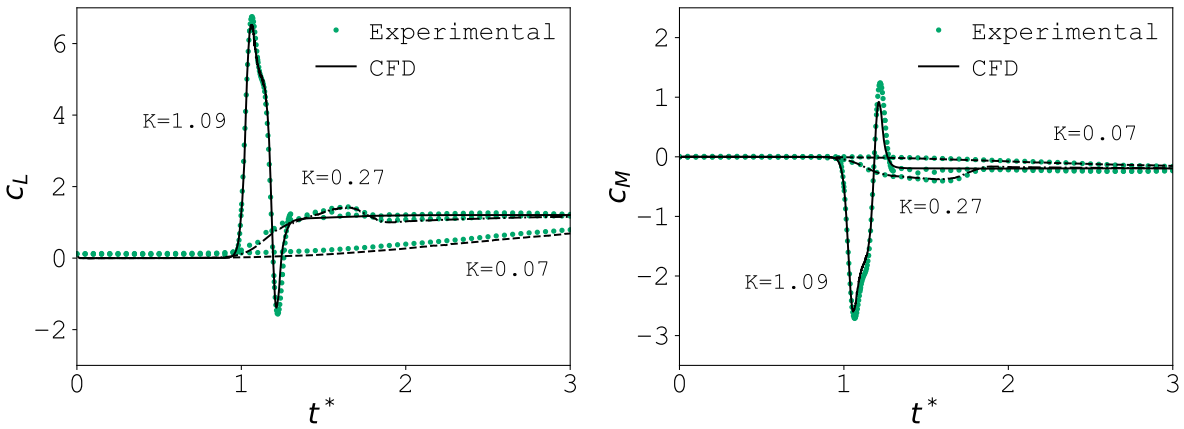

Fig. 5 Comparison of aerodynamic coefficients from CFD (curves) and experimental data (markers) for three rates of motion. Left graph shows lift, and right pitching moment

Experimental flow conditions were also replicated. With a free stream velocity of $U_\infty = 0.2$m/s, the Reynolds number based on the chord length is $Re = 4$ x 10^4.

A comparison of the aerodynamic coefficients obtained from CFD simulations and experimental results is presented in Fig. 5. A remarkably good agreement is noticed for all cases, encouraging the use of this CFD model as a validation tool for arbitrary camber variations of the discrete-vortex model.

From the original geometry, a new arrangement was derived to broaden the number of parameters defining morphing, like the flap length. A 30% total chord flap length was chosen following values from the literature on the topic [20], and observed in flapping-like means of locomotion in nature [18]. Results for both configurations are included in Sect. 4.

4 Results and discussion

In this section, the capability of MDVM in modeling temporal camber variations is assessed. On an airfoil translating at a constant velocity with zero angle of attack, flap kinematics are prescribed in the form of a sinusoidal wave:

$$\delta = \delta_{max} \sin(\omega t) \quad , \tag{30}$$

where δ_{max} is the amplitude of the motion (flap deflection); and ω the angular frequency, whose value here is twice that of the reduced frequency, k_δ.

Three sets of harmonic flap deflection cases are considered: small, medium and large amplitude. The selection of shape-control parameters for the last two sets was guided by biological bending patterns. The interested reader may refer to Ref. [32] for a detailed explanation on the reasoning. These parameters include the flap length (or flexion ratio, $\frac{c_f}{c}$), the deflection amplitude, and the reduced frequency. The latter was tailored to keep the Strouhal number within the optimal range seen in biological propulsion. This dimensionless number, which relates oscillatory and linear fluid velocities, can be expressed in terms of the deflection parameters as:

$$St_\delta = \frac{2k_\delta}{\pi} \frac{c_f}{c} \sin \delta_{max} \quad . \tag{31}$$

As for the small amplitude case, the objective is to prove that implementing the modified Kutta condition in the model enhances the estimation of aerodynamic loads. Values of each parameter defining the studied cases are collected in Table 1.

4.1 Small amplitude

Including the study of a small-amplitude flap deflection case does not aim so much to test the validity of a novel approach presented in this paper to model variable camber foils, but to rather highlight the effect that

Table 1 Parameters used to characterize trailing-edge flexion on studied cases

Case	Flexion ratio $\frac{c_f}{c}$	Amplitude δ_{max}	Reduced frequency k_δ	Strouhal number St_δ
A	0.5	1°	0.5	0.003
B	0.3	20°	π	0.21
C	0.5	20°	π	0.35
D	0.3	45°	$\pi/2$	0.21
E	0.5	45°	$\pi/2$	0.35

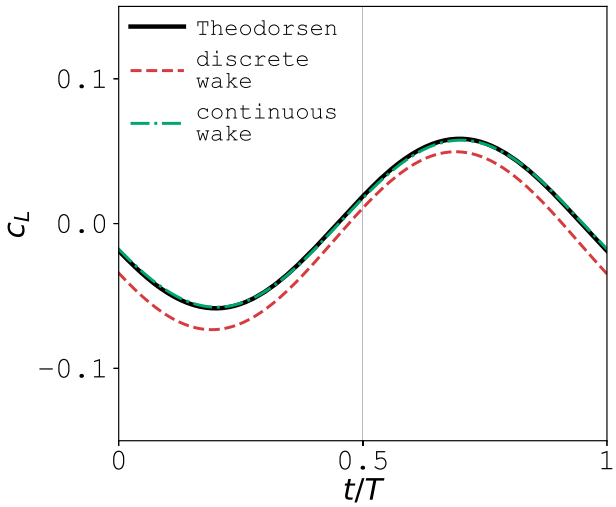

Fig. 6 Effect of wake vorticity modeling on lift coefficient: discrete vs continuous representation. Results are for *case A*

different wake modeling strategies have on the estimation of aerodynamic loads. For this purpose, the lift coefficient predicted with two different versions of the low-order model, using different distributions of wake vorticity, is compared against classical theory in Fig. 6 for one cycle of flap deflection. Kinematics parameters used are given by *case A* in Table 1. If the wake vorticity shed at the trailing edge in the current time step is represented by a continuous distribution, estimations of the lift coefficient made by MDVM and Theodorsen's classical theory are seen to perfectly match (dash-dotted and solid lines). This result was expected since the exact Wagner solution, which is an extension of Theodorsen's solution for non-harmonic motions, was used to derive the vorticity distribution. If, otherwise, the shed wake vorticity is formulated as a discrete distribution, by using regularized vortex blobs for example, as often observed in the literature [37,38], there is a discontinuity in the vortex sheet strength across the trailing edge, and the lift coefficient predicted by MDVM (dashed line) exhibits an offset when compared to the analytical solution (solid line).

All results presented in what follows have been obtained by adopting in MDVM the continuous representation of shed wake vorticity. Before proceeding to analyze the aerodynamic drag coefficient, it must be noticed that nonzero drag predictions are expected with MDVM despite being developed from inviscid flow theory. Owing to unsteady aerodynamics effects like body kinematics, shape variations, and wake vortices, the airflow near the airfoil is deflected, resulting in a non-viscous contribution to the drag force. For this first case, however, because of the very small deflection amplitude the above-mentioned contribution from the unsteadiness of the problem is minimal, as clearly shown in Fig. 7b. On the contrary, CFD simulations do account for viscosity in addition to calculating the potential contribution to drag, and so the computed force presents a larger value than the low-order model.

Just as it has been demonstrated for the lift coefficient in Fig. 6, which coincides with results shown in Fig. 7a, the pitching moment coefficient at the leading edge estimated with MDVM also matches the analytical solution from classical theory, as observed in Fig. 7c. Both curves are in excellent agreement with CFD results.

Vortex particles from MDVM and normalized out-of-plane vorticity contours extracted from CFD simulations are shown overlaid in Fig. 7d. The flap deflection amplitude of this case is not large enough for the wake to roll-up into vortices. The smooth wake oscillations are nevertheless properly reproduced by MDVM.

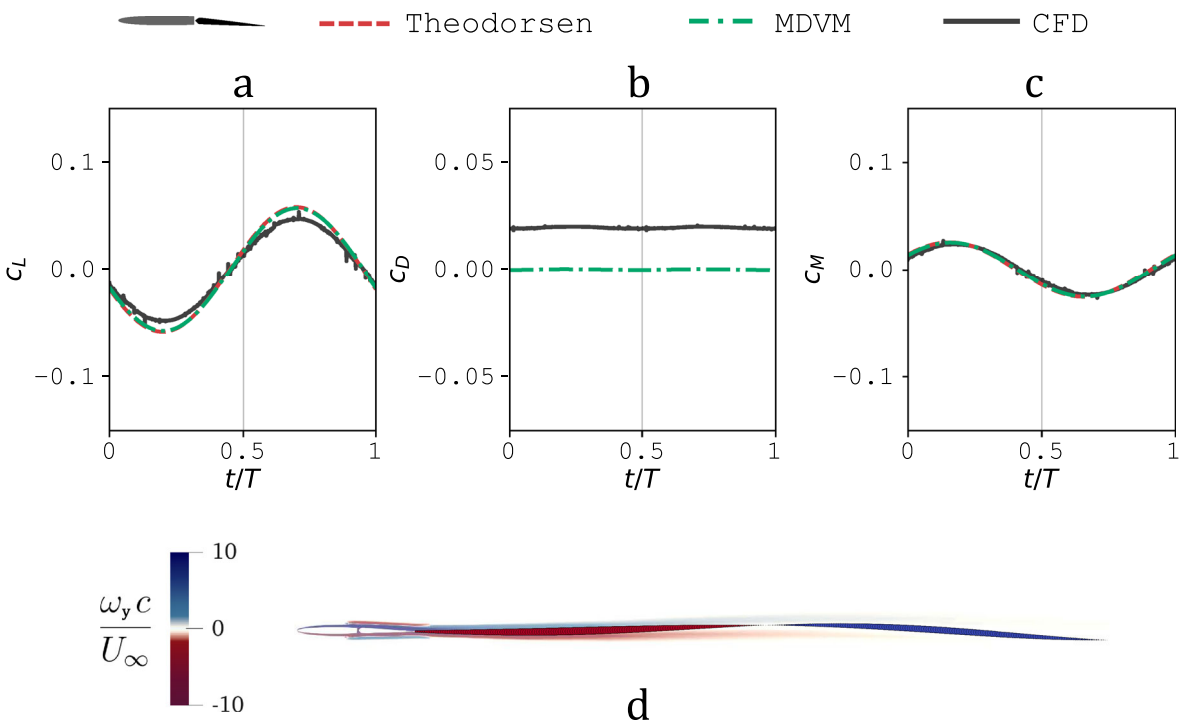

Fig. 7 Analysis of *case A*: lift coefficient **a**, drag coefficient **b**, pitching moment coefficient at the leading edge **c**, and flow visualization **d**. Kinematics parameters are: flexion ratio $c_f/c = 0.5$, amplitude $\delta_{max} = 1°$ and reduced frequency $k_\delta = 0.5$

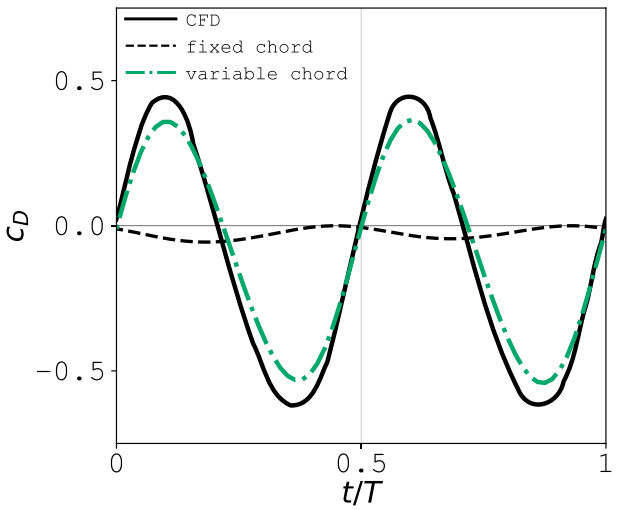

Fig. 8 Effect of chord line definition on drag coefficient: fixed vs time-varying. Results are for *case C*

4.2 Medium amplitude

Increasing the deflection amplitude or the reduced frequency produces larger values of potential drag on the immersed deforming body. The medium-amplitude flap deflection case is useful to showcase the disparity in drag estimation made by the two definitions of the chord line discussed in Sect. 2.1: fixed vs time-varying chord line.

To that end, a comparison between the drag coefficient predicted with both approaches and CFD computations is given in Fig. 8. Results shown correspond to kinematics parameters from *case C* in Table 1. If the fixed chord line approach is followed to construct the low-order model, a nearly zero-drag value is estimated (dashed line). It is interesting to note the negative sign of this magnitude for the complete cycle of flap deflec-

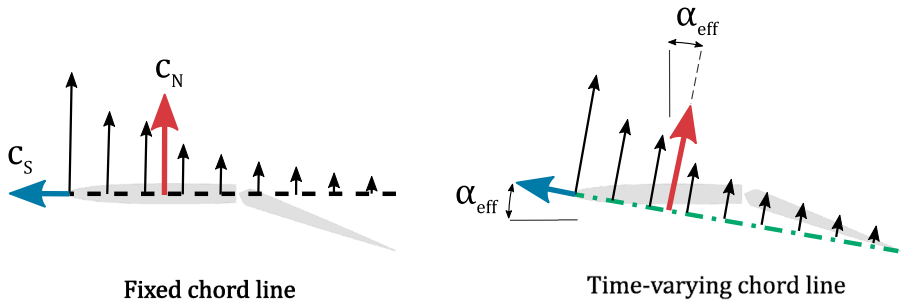

Fig. 9 Diagram of forces acting on an airfoil and their orientation relative to the incoming airflow: suction force (blue arrow) and pressure force (red arrow)

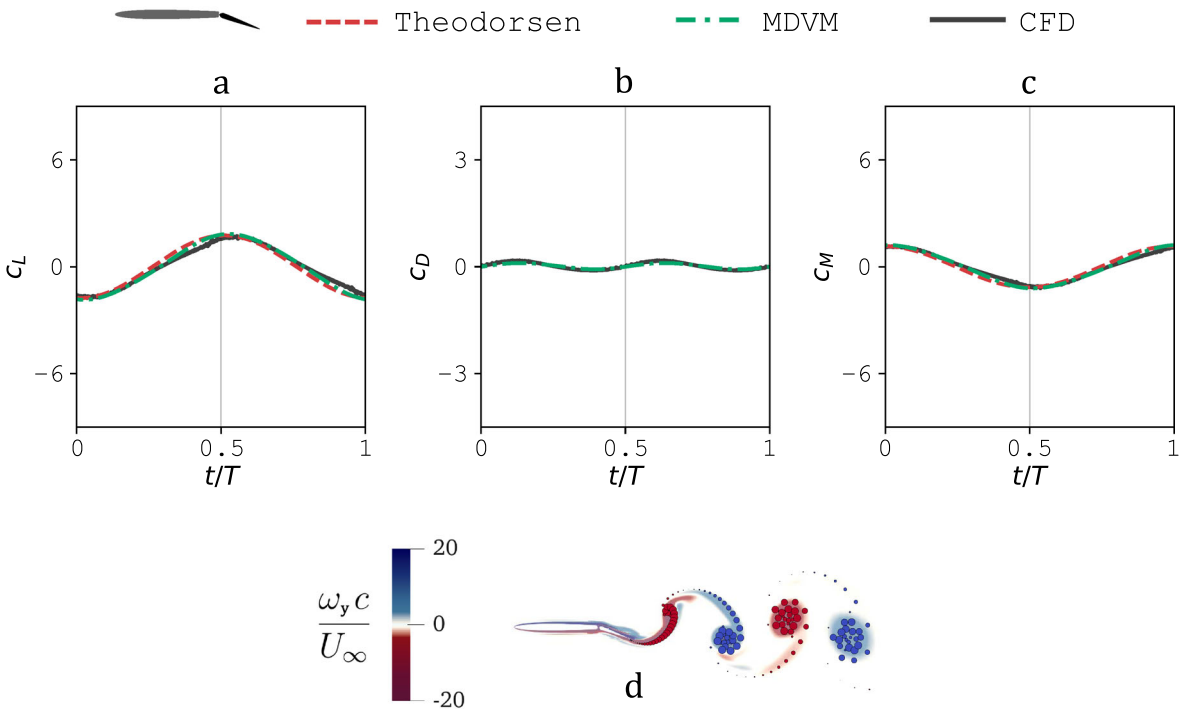

Fig. 10 Analysis of *case B*: lift coefficient **a**, drag coefficient **b**, pitching moment coefficient at the leading edge **c**, and flow visualization **d**. Kinematics parameters are: flexion ratio $c_f/c = 0.3$, amplitude $\delta_{max} = 20°$ and reduced frequency $k_\delta = \pi$

tion, meaning that pure thrust is generated with this approach. However, if the chord line is allowed to vary in time, as proposed in this work, drag predictions (dash-dotted line) get closer to the real value, tracking the CFD curve (solid line) with fair accuracy. The slightly smaller value was to be expected and is attributed to the viscous drag, which is only captured with the high fidelity simulation.

To better understand the differences observed between both approaches, we look at the orientation of force vectors relative to the incoming flow, schematized in Fig. 9. Integration of the unsteady pressure distribution (black arrows) along the chord line yields the pressure, or normal, force vector (red arrow). For the fixed chord line approach, this vector stands always perpendicular to the direction of motion since no pitch kinematics are considered in this paper, which means that only lift is generated. The sole contribution to drag is therefore owed to the suction force (blue arrow). Because this vector points into the direction of motion the generated drag is always negative, as is noticed in Fig. 8. On the contrary, allowing the chord line to rotate with flap deflections modifies the effective angle of attack in time. The pressure force vector is tilted producing both, lift and drag.

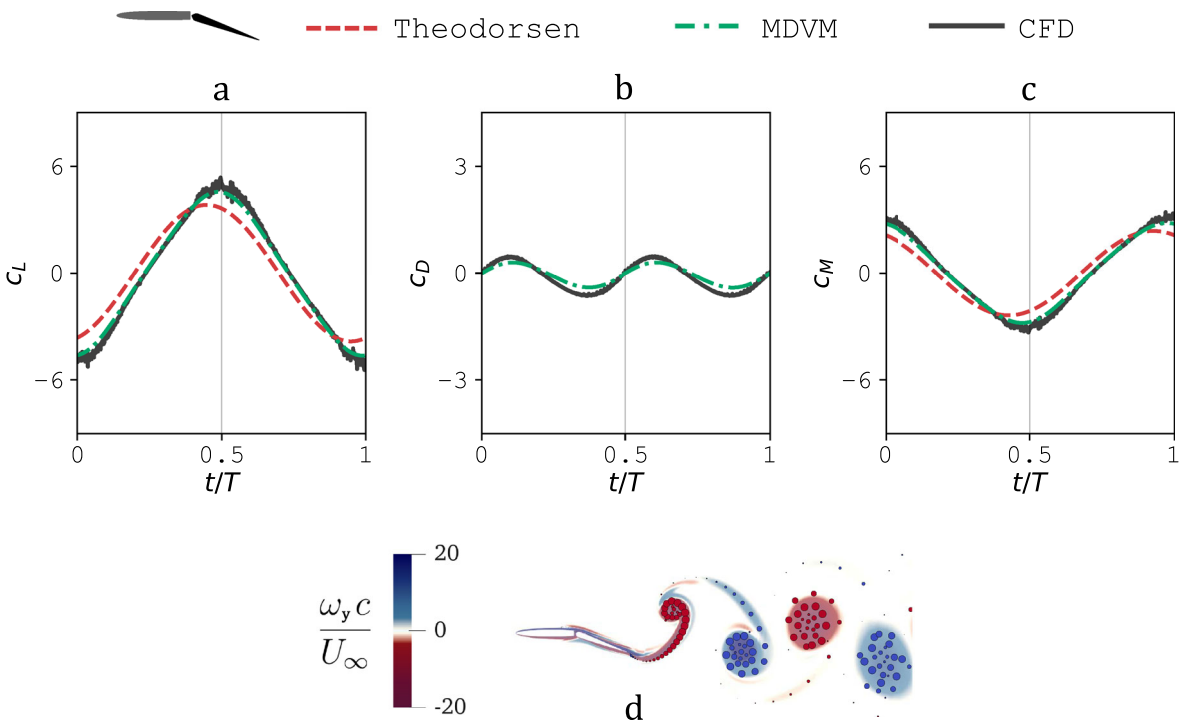

Fig. 11 Analysis of *case C*: lift coefficient **a**, drag coefficient **b**, pitching moment coefficient at the leading edge **c**, and flow visualization **d**. Kinematics parameters are: flexion ratio $c_f/c = 0.5$, amplitude $\delta_{max} = 20°$ and reduced frequency $k_\delta = \pi$

Results shown in the remainder of the paper have been obtained by implementing the variable chord line definition in MDVM. Aerodynamic coefficients for *case B* are analyzed in Fig. 10. For this medium-amplitude medium-length flap deflection case, both, the low-order model and the classical theory of Theodorsen, track CFD curves very closely.

Flow field representation through the spatial distribution of vorticity is displayed in Fig. 10d for two cycles of flap motion. Particles from the vortex model overlap normalized out-of-plane vorticity contours from high-fidelity computations. The deflection of a trailing-edge flap with the parameters given for this case imparts to the fluid a rotational motion strong enough for the wake to roll-up into vortices. During each cycle of flap deflection, two vortices are shed from the trailing edge with opposite sense of rotation, a vortex shedding pattern classified as 2S mode [53]. Those vortices rotating clockwise, with positive vorticity (blue colored in the figure), are situated below the wake center line; and those rotating counter-clockwise, with negative vorticity (red colored), above it. Vortices in this wake configuration organized in two rows, known as reverse Bénard-von Kármán vortex street, induce on each other a downstream velocity [22]. This thrust-indicative wake pattern is distinctive of flapping-based propulsion and has been observed on pure pitching and pure plunging airfoils [15]. MDVM captures the location and size of each vortex with great accuracy.

Larger values of the flexion ratio produce larger increments in the effective angle of attack for the same deflection amplitude, as it is clear from Eq. (3). The aerodynamic coefficients for *case C* in Table 1, where the flexion ratio is $\frac{c_f}{c} = 0.5$, are depicted in Fig. 11. Analytical results, obtained under the small-perturbations assumption, differ in magnitude and in phase when compared to the viscous flow calculations, whereas MDVM estimations keep a good agreement.

4.3 Large amplitude

Further increasing the amplitude of flap deflection, the characteristic sinusoidal waveform of the aerodynamic coefficients temporal evolution for small-medium amplitudes begins to distort. This behavior is noticed in Fig. 12 for *case D*, and in Fig. 13 for *case E*. For the shortest flap length case, the distortion of aerodynamic coefficients is more pronounced in CFD calculations than in analytical and numerical estimations, as evidenced in Fig. 12. The observed dissimilarity between curves might be a consequence of flow separation. From the

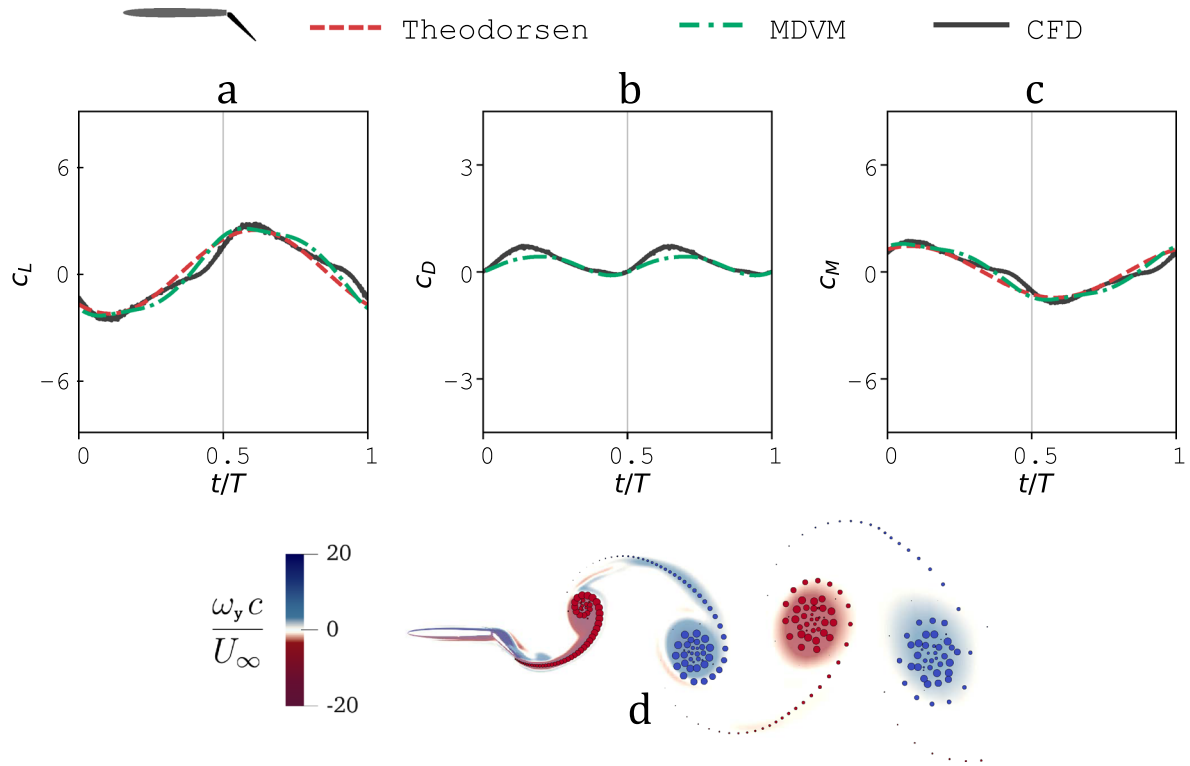

Fig. 12 Analysis of *case D*: lift coefficient **a**, drag coefficient **b**, pitching moment coefficient at the leading edge **c**, and flow visualization **d**. Kinematics parameters are: flexion ratio $c_f/c = 0.3$, amplitude $\delta_{max} = 45°$, reduced frequency $k_\delta = \pi/2$

CFD vorticity contours displayed in Fig. 12d, separation is seen to occur over the trailing-edge flap, and the hinge gap seems to be the source of separation. Because the geometry for the classical theory and MDVM does not present a discontinuity in this region, aerodynamic coefficients are expected to differ to some extent.

Finally, large flexion ratios in combination with large amplitudes of flap deflection result in an effective angle of attack large enough to trigger leading-edge flow separation. This is illustrated through the vorticity contour extracted from CFD in Fig. 13d. Modeling of leading-edge vorticity shedding has not been treated in the development of MDVM, neither is it accounted for in classical theory. In terms of aerodynamic coefficients, the low-order model successfully reproduces CFD results nonetheless, as Fig. 13 shows. On the contrary, analytical predictions differ in shape and magnitude. In this case, however, the timing of peaks on the curves is well captured, presumably due to the lower reduced frequency.

Visualization of the flow field through vorticity contours for *case D* and *case E* reveals a propulsive vortical signature in the wake. This is, a similar arrangement of vortices to that of *case B* and *case C*, with slightly increased separation between vortex pairs (see Figs. 12d and 13d). In spite of MDVM not modeling flow separation at the leading edge its effect on shed vortices seems to be minor, and the low-order model properly reproduces the wake pattern, both the location and the size of vortices.

5 Conclusion

A computationally inexpensive predictive tool has been developed in this paper to simulate the unsteady flow response to foils undergoing temporal variations of the camber, which are caused by deflection of a trailing-edge flap. This low-order model combines potential-flow theory adapted for unsteady airfoils with a numerical method using discrete-vortex elements. In pursuance of attaining camber variations of large amplitude, a new definition of the chord line is proposed in this paper to avoid the restriction of thin-airfoil theory to small flow disturbances. A time-varying chord line is defined between the instantaneous position of the leading edge and the trailing edge. The zero-normal flow boundary condition is then transferred from the camber line to this effective chord line, which varies in time due to flap motion. The maximum distance between these curves (camber ratio) is thus reduced, and therefore, the error associated with such simplification.

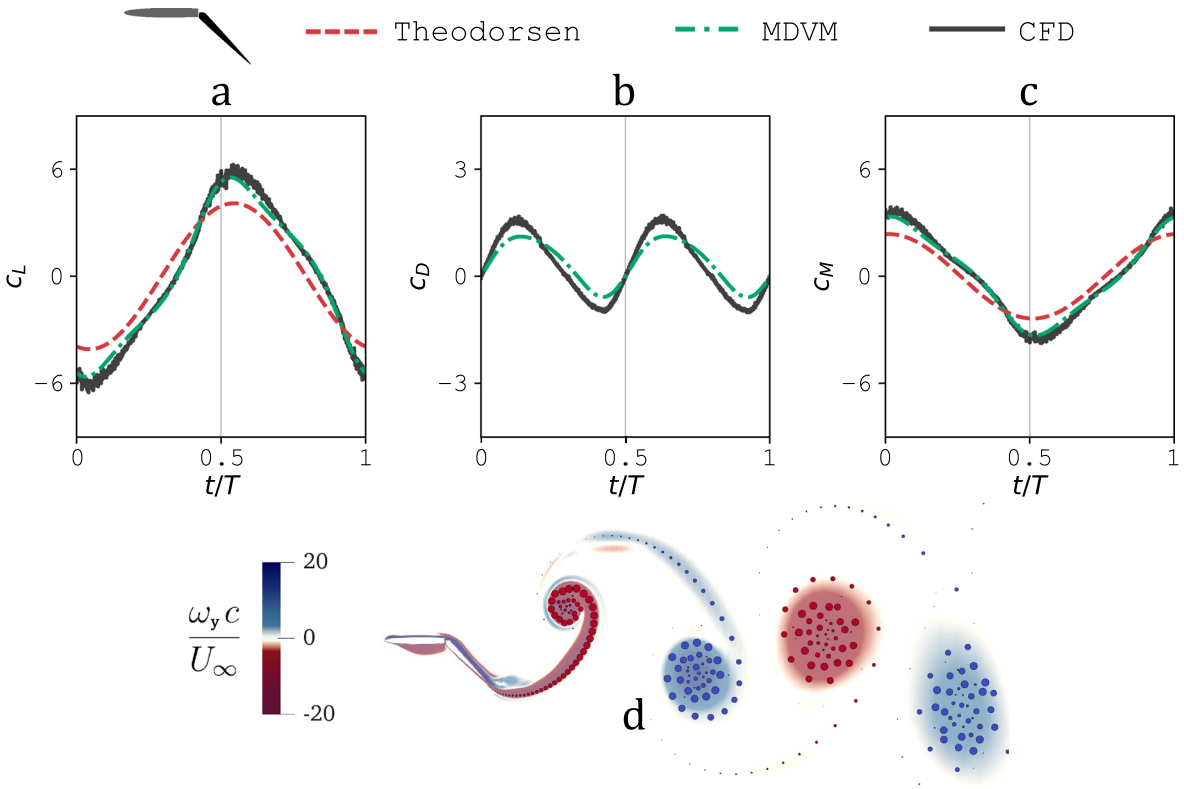

Fig. 13 Analysis of *case E*: lift coefficient **a**, drag coefficient **b**, pitching moment coefficient at the leading edge **c**, and flow visualization **d**. Kinematics parameters are: flexion ratio $c_f/c = 0.5$, amplitude $\delta_{max} = 45°$, reduced frequency $k_\delta = \pi/2$

The performance of the new morphing discrete-vortex model has been assessed through a set of harmonic trailing-edge deflection cases. These cases have been designed by combining shape-control parameters like the flexion ratio, the amplitude and the rate of deflection. Predictions from classical aerodynamic theory, as well as CFD calculations, have been included in the analysis. The main discussion was centered around the drag force, where differences are more pronounced both, between MDVM and CFD, and between keeping the chord line fixed or allowing it to vary in time. Drag predictions by the low-order model are slightly lower than CFD calculations, which is attributed to the viscous component of drag force not being captured with this potential-flow based model. The enhancement in aerodynamic loads prediction with a time-varying chord line is explained through the orientation of the pressure force vector: allowing the chord line to rotate with flap deflections the effective angle of attack is varied in time, tilting the normal force vector against the incoming free stream to produce both, lift and drag. As for the temporal evolution of lift and moment coefficients, MDVM estimations strongly match CFD computations. This is of special relevance for the large-amplitude deflection cases, where the characteristic sine waveform of harmonic motions starts to distort, which the classical theory cannot predict. The ability of MDVM to model wake roll-up is evinced through visualization of the flow field by vorticity contours, showing a great accuracy in the location and size of vortices shed from the trailing edge.

In short, this physics-based low-order model is capable of simulating unsteady flows due to variable-camber foils with fairly high levels of accuracy, and run-times on the order of seconds on a personal laptop. It lays the groundwork for modeling of morphing foils with more complex camber distributions.

Acknowledgements This work was supported by the UK Engineering and Physical Sciences Research Council [grant numbers EP/N509668/1, EP/R513222/1]. The authors gratefully acknowledge Dr. Albert Medina (AFRL/RQVA) for the data used in the CFD geometry.

Open Access This article is licensed under a Creative Commons Attribution 4.0 International License, which permits use, sharing, adaptation, distribution and reproduction in any medium or format, as long as you give appropriate credit to the original author(s) and the source, provide a link to the Creative Commons licence, and indicate if changes were made. The images or other third party material in this article are included in the article's Creative Commons licence, unless indicated otherwise in a credit

line to the material. If material is not included in the article's Creative Commons licence and your intended use is not permitted by statutory regulation or exceeds the permitted use, you will need to obtain permission directly from the copyright holder. To view a copy of this licence, visit http://creativecommons.org/licenses/by/4.0/.

Author contributions AMC developed the mathematical model, ran the simulations, analyzed the results, prepared the figures and wrote the manuscript; KR participated in the initial design of the study, supervised the research and reviewed the final manuscript.

Declarations

Conflict of interest No competing interests.

Ethics approval and consent to participate Not applicable.

Consent for publication All authors gave their final approval for publication.

References

1. Ajanic, E., Paolini, A., Coster, C., Floreano, D., Johansson, C.: Robotic avian wing explains aerodynamic advantages of wing folding and stroke tilting in flapping flight. Adv. Intell. Syst. **5**(2), 2200148 (2023). https://doi.org/10.1002/aisy.202200148
2. Ansari, S., Żbikowski, R., Knowles, K.: Non-linear unsteady aerodynamic model for insect-like flapping wings in the hover part 2: implementation and validation. Proc. Inst. Mech. Eng. Part G J. Aerosp. Eng. **220**(3), 169–186 (2006). https://doi.org/10.1243/09544100JAERO50
3. Chang, E., Matloff, L., Stowers, A., Lentink, D.: Soft biohybrid morphing wings with feathers underactuated by wrist and finger motion. Sci. Robot. **5**(38), eaay1246 (2020). https://doi.org/10.1126/scirobotics.aay1246
4. Cheney, J., Rehm, J., Swartz, S., Breuer, K.: Bats actively modulate membrane compliance to control camber and reduce drag. J. Exp. Biol. **225**(14), 1–6 (2022). https://doi.org/10.1242/jeb.243974
5. Cheney, J., Stevenson, J., Durston, N., Maeda, M., Song, J., Megson-Smith, D., Windsor, S., Usherwood, J., Bomphrey, R.: Raptor wing morphing with flight speed. J. R. Soc. Interface **18**(180), 20210349 (2021). https://doi.org/10.1098/rsif.2021.0349
6. Chorin, A.: Numerical study of slightly viscous flow. J. Fluids Mech. **57**(4), 785–796 (1973). https://doi.org/10.1017/S0022112073002016
7. Chorin, A., Bernard, P.: Discretization of a vortex sheet, with an example of roll-up. J. Comput. Phys. **13**(3), 423–429 (1973). https://doi.org/10.1016/0021-9991(73)90045-4
8. Clements, R.: An inviscid model of two-dimensional vortex shedding. J. Fluids Mech. **57**(2), 321–336 (1973). https://doi.org/10.1017/S0022112073001187
9. Clements, R., Maull, D.: The representation of sheets of vorticity by discrete vortices. Prog. Aerosp. Sci. **16**(2), 129–146 (1975). https://doi.org/10.1016/0376-0421(75)90013-5
10. Colorado, J., Barrientos, A., Rossi, C., Breuer, K.S.: Biomechanics of smart wings in a bat robot: morphing wings using SMA actuators. Bioinspir. Biomim. **7**(3), 036006 (2012). https://doi.org/10.1088/1748-3182/7/3/036006
11. Cottet, G.H., Koumoutsakos, P.: Vortex Methods: Theory and Practice, vol. 8. Cambridge University Press, Cambridge (2000)
12. Darakananda, D., Eldredge, J.: A versatile taxonomy of low-dimensional vortex models for unsteady aerodynamics. J. Fluids Mech. **858**, 917–948 (2019). https://doi.org/10.1017/jfm.2018.792
13. Eldredge, J., Jones, A.: Leading-edge vortices: mechanics and modeling. Ann. Rev. Fluids Mech. **51**(1), 75–104 (2019). https://doi.org/10.1146/annurev-fluid-010518-040334
14. Faure, T., Dumas, L., Montagnier, O.: Numerical study of two-airfoil arrangements by a discrete vortex method. Theor. Comput. Fluids Dyn. **34**(1), 79–103 (2020). https://doi.org/10.1007/s00162-019-00511-0
15. Freymuth, P.: Propulsive vortical signature of plunging and pitching airfoils. AIAA J. **26**(7), 881–883 (1988). https://doi.org/10.2514/3.9982
16. Greenshields, C.: OpenFOAM v11 User Guide. The OpenFOAM Foundation, London, UK (2023)
17. Hammer, P., Altman, A., Eastep, F.: Validation of a discrete vortex method for low Reynolds number unsteady flows. AIAA J. **52**(3), 643–649 (2014). https://doi.org/10.2514/1.J052510
18. Hang, H., Heydari, S., Costello, J., Kanso, E.: Active tail flexion in concert with passive hydrodynamic forces improves swimming speed and efficiency. J. Fluids Mech. **932**, A35 (2022). https://doi.org/10.1017/jfm.2021.984
19. Harvey, C., Gamble, L., Bolander, C., Hunsaker, D., Joo, J., Inman, D.: A review of avian-inspired morphing for UAV flight control. Prog. Aerosp. Sci. **132**, 100825 (2022). https://doi.org/10.1016/j.paerosci.2022.100825
20. He, G., Deparday, J., Siegel, L., Henning, A., Mulleners, K.: Stall delay and leading-edge suction for a pitching airfoil with trailing-edge flap. AIAA J. **58**(12), 5146–5155 (2020). https://doi.org/10.2514/1.J059719
21. Jasak, H., Jemcov, A., Tukovic, Z., et al.: Openfoam: A c++ library for complex physics simulations. In: International Workshop on Coupled Methods in Numerical Dynamics, vol. 1000, pp. 1–20 (2007)
22. Jones, K., Dohring, C., Platzer, M.: Experimental and computational investigation of the Knoller–Betz effect. AIAA J. **36**(7), 1240–1246 (1998). https://doi.org/10.2514/2.505
23. Kamrani Fard, K., Ngo, V., Liburdy, J.: A leading-edge vortex initiation criteria for large amplitude foil oscillations using a discrete vortex model. Phys. Fluids **33**(11), 115123 (2021). https://doi.org/10.1063/5.0065097
24. Katz, J.: A discrete vortex method for the non-steady separated flow over an airfoil. J. Fluids Mech. **102**, 315–328 (1981)
25. Katz, J., Plotkin, A.: Low-Speed Aerodynamics, vol. 13. Cambridge University Press, Cambridge (2001)
26. Kiya, M., Arie, M.: A contribution to an inviscid vortex-shedding model for an inclined flat plate in uniform flow. J. Fluids Mech. **82**(2), 223–240 (1977). https://doi.org/10.1017/S0022112077000627

27. Kuwahara, K.: Numerical study of flow past an inclined flat plate by an inviscid model. J. Phys. Soc. Jpn. **35**(5), 1545–1551 (1973). https://doi.org/10.1143/JPSJ.35.1545
28. Leonard, A.: Vortex methods for flow simulation. J. Comput. Phys. **37**(3), 289–335 (1980). https://doi.org/10.1016/0021-9991(80)90040-6
29. Liu, Z., Lai, J., Young, J., Tian, F.B.: Discrete vortex method with flow separation corrections for flapping-foil power generators. AIAA J. **55**(2), 410–418 (2017). https://doi.org/10.2514/1.J055267
30. Maeda, M., Nakata, T., Kitamura, I., Tanaka, H., Liu, H.: Quantifying the dynamic wing morphing of hovering hummingbird. R. Soc. Open Sci. **4**(9), 170307 (2017). https://doi.org/10.1098/rsos.170307
31. Manar, F., Jones, A.: Evaluation of potential flow models for unsteady separated flow with respect to experimental data. Phys. Rev. Fluids **4**(3), 034702 (2019). https://doi.org/10.1103/PhysRevFluids.4.034702
32. Martínez-Carmena, A.: Vortex Flows Around Morphing Foils. University of Glasgow, Glasgow (2023)
33. Medina, A., Ol, M., Mancini, P., Jones, A.: Revisiting conventional flaps at high deflection rate. AIAA J. **55**(8), 2676–2685 (2017). https://doi.org/10.2514/1.J055754
34. Moore, D.: The Discrete Vortex Approximation of a Finite Vortex Sheet. California Institute of Technology, Pasadena (1971)
35. Muijres, F., Johansson, C., Barfield, R., Wolf, M., Spedding, G., Hedenström, A.: Leading-edge vortex improves lift in slow-flying bats. Science **319**(5867), 1250–1253 (2008). https://doi.org/10.1126/science.1153019
36. Ramesh, K.: On satisfying the kutta condition in unsteady thin Aerofoil theory (2022). arXiv preprint arXiv:2205.08647
37. Ramesh, K., Gopalarathnam, A., Edwards, J., Ol, M., Granlund, K.: An unsteady airfoil theory applied to pitching motions validated against experiment and computation. Theor. Comput. Fluids Dyn. **27**(6), 843–864 (2013). https://doi.org/10.1007/s00162-012-0292-8
38. Ramesh, K., Gopalarathnam, A., Granlund, K., Ol, M., Edwards, J.: Discrete-vortex method with novel shedding criterion for unsteady Aerofoil flows with intermittent leading-edge vortex shedding. J. Fluids Mech. **751**, 500–538 (2014). https://doi.org/10.1017/jfm.2014.297
39. Ramesh, K., Murua, J., Gopalarathnam, A.: Limit-cycle oscillations in unsteady flows dominated by intermittent leading-edge vortex shedding. J. Fluids Struct. **55**, 84–105 (2015). https://doi.org/10.1016/j.jfluidstructs.2015.02.005
40. Rosenhead, L., Jeffreys, H.: The formation of vortices from a surface of discontinuity. Proc. R. Soc. Lond. **134**(823), 170–192 (1931). https://doi.org/10.1098/rspa.1931.0189
41. Rossi, C., Colorado, J., Coral, W., Barrientos, A.: Bending continuous structures with SMAs: a novel robotic fish design. Bioinspir. Biomim. **6**(4), 045005 (2011). https://doi.org/10.1088/1748-3182/6/4/045005
42. Saffman, P., Baker, G.: Vortex interactions. Ann. Rev. Fluids Mech. **11**(1), 95–121 (1979). https://doi.org/10.1146/annurev.fl.11.010179.000523
43. Sarpkaya, T.: An analytical study of separated flow about circular cylinders. J. Basic Eng. **90**(4), 511–518 (1968). https://doi.org/10.1115/1.3605180
44. Sarpkaya, T.: An inviscid model of two-dimensional vortex shedding for transient and asymptotically steady separated flow over an inclined plate. J. Fluids Mech. **68**(1), 109–128 (1975). https://doi.org/10.1017/S0022112075000717
45. Sedky, G., Lagor, F., Jones, A.: Unsteady aerodynamics of lift regulation during a transverse gust encounter. Phys. Rev. Fluids **5**(7), 074701 (2020). https://doi.org/10.1103/PhysRevFluids.5.074701
46. Spalart, P.: Vortex methods for separated flows. VKI Comput. Fluid Dyn. **1**, 66 (1988)
47. Suresh Babu, A., Medina, A., Rockwood, M., Bryant, M., Gopalarathnam, A.: Theoretical and experimental investigation of an unsteady airfoil in the presence of external flow disturbances. J. Fluid Mech. **921**, A21 (2021). https://doi.org/10.1017/jfm.2021.484
48. Suresh Babu, A., Narsipur, S., Bryant, M., Gopalarathnam, A.: Leading-edge-vortex tailoring on unsteady airfoils using an inverse aerodynamic approach. Phys. Fluids **34**(5), 057107 (2022). https://doi.org/10.1063/5.0090328
49. Takami, H.: Numerical Experiment with Discrete Vortex Approximation, with Reference to the Rolling Up of a Vortex Sheet. Stanford University, Stanford (1964)
50. Vatistas, G., Kozel, V., Mih, W.: A simpler model for concentrated vortices. Exp. Fluids **11**(1), 73–76 (1991). https://doi.org/10.1007/BF00198434
51. Von Busse, R., Hedenström, A., Winter, Y., Johansson, C.: Kinematics and wing shape across flight speed in the bat, leptonycteris yerbabuenae. Biol. Open **1**(12), 1226–1238 (2012). https://doi.org/10.1242/bio.20122964
52. Wang, C., Eldredge, J.: Low-order phenomenological modeling of leading-edge vortex formation. Theor. Comput. Fluid Dyn. **27**(5), 577–598 (2013). https://doi.org/10.1007/s00162-012-0279-5
53. Williamson, C., Roshko, A.: Vortex formation in the wake of an oscillating cylinder. J. Fluids Struct. **2**(4), 355–381 (1988). https://doi.org/10.1016/S0889-9746(88)90058-8
54. Wolf, M., Johansson, C., von Busse, R., Winter, Y., Hedenström, A.: Kinematics of flight and the relationship to the vortex wake of a Pallas' long tongued bat (Glossophaga soricina). J. Exp. Biol. **213**(12), 2142–2153 (2010). https://doi.org/10.1242/jeb.029777
55. Wolf, T., Konrath, R.: Avian wing geometry and kinematics of a free-flying barn owl in flapping flight. Exp. Fluids **56**(2), 1–18 (2015). https://doi.org/10.1007/s00348-015-1898-6
56. Xia, X., Mohseni, K.: Lift evaluation of a two-dimensional pitching flat plate. Phys. Fluids **25**(9), 091901 (2013). https://doi.org/10.1063/1.4819878

Publisher's Note Springer Nature remains neutral with regard to jurisdictional claims in published maps and institutional affiliations.